scientific reports

Check for updates

OPEN

Optical signature of retinal Tau fibrillation

Zita Salajková[1,6]✉, Lorenzo Barolo[2]✉, Paola Baiocco[2], Barbara Ruzicka[3,7], Francesco Mura[4], Francesco Di Lorenzo[5], Alberto Boffi[1,2], Vincenzo Ricco[6], Giancarlo Ruocco[1,7] & Marco Leonetti[1,6,8]

Fibrillated Tau proteins are believed to be a signature of Alzheimer's disease (AD) and may be potentially employed as a biosensor for AD early detection. Several studies revealed the presence of Tau accumulation and aggregation in the retina, similar to that observed in the brains of individuals with AD. These retinal changes can be non-invasively visualised through AD-related scores derived from reflectance measurements of the patient fundus. However, a direct link with the optical properties of fibrillated protein clusters is still lacking. Here, we present a new optical technique which measures the scattering optical properties of protein fibrils. Our experimental findings show that the scattering intensity of Tau has a wavelength dependence correlated to their size. The optical signal qualitatively replicates the spectral signature observed in human AD patient retinas. Our paper shows that the Tau protein spectral signature is compatible with the distinctive spectral signature of the AD, further confirming that retinal investigation is a promising tool.

Keywords Tau protein, Protein fibrillation monitoring, Alzheimer's disease, Side-scattering spectroscopy

Protein fibrillation, the aggregation of misfolded proteins into insoluble fibrils, is a pathological hallmark of several neurodegenerative diseases, which are indeed also called proteinopathies, such as Alzheimer's disease (AD), Frontotemporal Dementia, Lewy body dementia and Parkinson Disease. As the disease progresses, specific protein fibrils accumulate in distinct brain areas, leading to a cascade of physiopathological events which ultimately cause cellular dysfunction, neuronal loss and brain damage. This characteristic pathological process is primarily caused by the misfolding and aggregation of specific proteins into abnormal, toxic species in the central nervous system (CNS)[1]. In AD, we can observe amyloid-beta (Aβ) aggregation and accumulation of neurofibrillary tangles (NFTs) and paired helical filaments (PHFs), insoluble forms of tau protein[2].

The process of fibril accumulation starts many years before the disease symptom onset for both Aβ and tau protein[3]. Thus, the detection of these pathological abnormalities might serve as a disease biomarker in its early stage, even before the onset of cognitive symptoms[4,5]. Indeed, the current diagnostic methods, such as magnetic resonance imaging (MRI), positron emission tomography (PET), and measurement of cerebrospinal fluid (CSF) by lumbar puncture[6–8] are not suitable for routine population screening, as they are costly or invasive[9]. Therefore, by the time the patient is diagnosed with AD, the irreversible pathological cascade has already extensively affected brain functions, significantly reducing the eventual efficacy of a potentially beneficial disease-modifying treatment. As a result, the existing medications can only soften the symptoms for patients and ease the burden for the caregivers but do not substantially affect the rate of cognitive decline[10].

Recent studies suggested that the detection of protein aggregation in the human retina is a promising AD biomarker, as the retina is the only part of CNS that can be visualised non-invasively in vivo. Clinical and postmortem studies revealed that NFTs and PHFs found in the retina correlate with the amount measured in the brain[11–13]. Moreover, mirroring other biomarkers' patterns, these biochemical alterations were observed in the retina nearly 10–20 years before the patient's cognitive decline, potentially enabling AD diagnosis in the preclinical stage[14–16]. The ability to directly visualise the retina and its shared neurobiology with the brain suggested that ophthalmoscopic investigation is a promising target for developing a test for detecting

[1]Center for Life Nano- and Neuro-Science, Istituto Italiano di Tecnologia, Viale Regina Elena 291, 00161 Rome, Italy. [2]Department of Biochemical Sciences "Alessandro Rossi Fanelli", Sapienza University of Rome, P.le A. Moro 5, 00185 Rome, Italy. [3]Sapienza Unit, Institute for Complex Systems of the National Research Council (ISC-CNR), Piazzale A. Moro 5, 00185 Rome, Italy. [4]Research Center on Nanotechnologies Applied to Engineering of Sapienza (CNIS), P.zza Aldo Moro 5, 00185 Rome, Italy. [5]Neuropsychophisiology Lab, Istituto Di Ricovero E Cura a Carattere Scientifico Santa Lucia, via Ardeatina 306, 00179 Rome, Italy. [6]D-Tails s.r.l. BCorp, Via di Torre Rossa, 66, 00165 Rome, Italy. [7]Dipartimento di Fisica, Università di Roma "La Sapienza", P.le Aldo Moro 5, 00185 Rome, Italy. [8]Rome Unit, Institute of Nanotechnology of the National Research Council of Italy, CNR-NANOTEC, Piazzale A. Moro 5, 00185 Rome, Italy. ✉email: zita.salajkova@iit.it; lorenzo.barolo@uniroma1.it

disease-related biomarkers in the earliest stages of preclinical AD[17–20]. The first in vivo visualisation of the AD retina was performed on transgenic murine models[21–23]. In this study, the amyloid plaques were stained with curcumin, a natural and safe fluorochrome with high affinity and specificity of binding to the Aβ fibrils. Later, this method was tested in the human cohort of AD patients[20]. The highly bioavailable Longvida curcumin was orally administered to the patients, and the retina was visualised by confocal scanning laser ophthalmoscope. The study demonstrated the feasibility of non-invasive Aβ plaque detection in the human retina, and subsequent proof-of-concept clinical trials confirmed the possibility of detecting a significant increase in retinal amyloid burden in AD patients compared with age-matched healthy controls.

More recently, hyperspectral imaging (HSI) was proposed as a potential method for AD early diagnosis as it has been shown that AD retinas have a specific wavelength-dependent effect on light scatter, the so-called "Spectral signature" that can be detected by HSI[24,25]. Compared to previously used fluorescence ophthalmoscopic methods, HSI does not require fluorescent staining. A study on AD animal model comparing retinal HSI of double transgenic (AD-associated APP and PS1 mutations) and wild-type mice (WT) shows that the HSI images of brains and retinas possess spectral signatures that allow distinguish between AD and WT mice even in the early asymptomatic stage[25]. Moreover, this study demonstrates that the spectral variation enabling the classification occurs at specific wavelengths, between 450 and 580 nm, for both the brain and retina[25]. In the next step, the possibility of early detection of AD by HSI was tested on double transgenic Alzheimer's mice in vivo by hyperspectral endoscopy[15]. Here, the spectral signature was modelled by convoluting the function representing haemoglobin light absorption appearing at 550 nm and Rayleigh light scattering and was attributed to the Aβ deposition. In the next step, the insights gained during animal model investigation were applied to studies on human AD subjects[24]. The spectral signature of the human retina measured in vivo was correlated with cognitive impairment level tested by mini-mental state examination revealing increasing retina optical density as a disease progress. The spectral signature was assigned to Rayleigh scattering of an increased concentration of ordered Aβ aggregates (prior to their deposition as insoluble plaques) despite the Aβ levels of subjects participating in the study being unknown. A similar study performed on patients diagnosed with AD neuropsychological test and PET images showing moderate-high Aβ burden demonstrates that AD patients could be distinguished from control subjects by analysing HSI retina images with the use of an advanced data processing method[19]. Although these results look promising, the direct link between this retinal reflectance spectral signature and the presence of protein fibrils is still lacking[18,26,27].

In this study, we present the Light Scattering Spectroscopy (LSS) instrument tailored to study the scattering properties of protein fibrils. LSS has gained interest as a medical diagnostic tool for its ability to detect early changes in tissue that might indicate cancer or other diseases[28–31]. During the presented investigation, LSS offers a more focused and detailed view of the scattering events specific to individual fibrils compared to HSI. Compared to previous studies that reported the reflection or absorption spectrum, our setup directly detects light scattering on particles in the solution. This approach enables us to capture the scattering signature of protein fibrils, targeting less explored fibrils of the microtubule-binding region (residues 244 to 372), usually referred as the K18 domain of Tau protein, which is crucial for enhancing our understanding of the scattering phenomena observed in the retinas of AD patients. In our set-up, a broad-wavelength light source illuminates scattering particles in solution, replicating a light source in the spectral range of commercial ophthalmoscopes; thus, the study aims to observe the scattering spectra of the pathological protein fibrils that can be compared to in vivo HSI observations. In this way, the LSS monitoring of protein fibrillation by analysing the wavelength-dependent scattering behaviour provides a missing connection between the reflectance spectrum signature of AD-affected retina and protein fibril scattering properties.

Results

BSA as a model of protein fibrillation

The spectroscopic measurement was conducted by bench side-scattering spectroscope using a light source with a broad wavelength range comparable to the common ophthalmoscopes. The instrument measures the side-scattering spectrum of particles in microliter-scale sample solutions quantified as total side-scattering power Ω (see the measurement on PS beads in Materials and Methods). The side-scattering configuration enables the determination of the optical properties of the molecular system, separating it from the contribution of specular reflection. The first part of the study aims to measure Ω of biological systems to explore how the size of clusters influences the wavelength dependence of light scattering. We employed solutions containing fixed concentrations of bovine serum albumin (BSA) at various aggregation stages. BSA was selected as a model sample due to its controllable, facile, and prompt formation of aggregates under elevated temperature. Therefore, the results can be easily associated with the properties of the aggregate (number and size).

For the purpose of our study, a set of six diverse sample solutions was prepared, each subjected to varying aggregation durations: 0, 0.5, 1, 3, 5, and 6.5 h at a temperature of 63 °C[32]. Prior to the spectral analysis, the solutions were characterised by standard techniques to describe the significant structural insights of the biological macromolecules under these experimental conditions. So later, we can explore their signature in the side scattering spectrum.

At first, the parameters such as hydrodynamic diameter, polydispersity, and the existence of protein aggregates in solution were measured by Dynamic Light Scattering (DLS) at different aggregation time points. Before the start of aggregation t = 0, the average hydrodynamic radius of BSA was (4.43 ± 0.03) nm; after 0.5 h, the measured radius increased to (6.7 ± 0.5) nm, and after 5 h to (10.9 ± 0.7) nm. These measurements confirmed the formation of aggregates and their growth. The measurements were performed directly on samples in solution in dilute conditions, with a concentration of 1 mg/mL, and repeated several times, and they are in line with the results present in the literature[33–35]. The analysis also indicates that the samples are highly monodisperse for t = 0 while not only the dimensions but also the polydispersity of the aggregates increases with time.

To further characterise the structural properties, the samples were visualised by Scanning Transmission Electron Microscopy (STEM) imaging, Fig. 1a–c. After 30 min at 63 °C, BSA already shows a high degree of fibrillation. Small fibrils start to populate the sample, and bigger clusters of aggregates are visible, even if not predominant in the whole sample. On the other hand, after 5 h, the heavy aggregates were omnipresent, infesting the whole solution. The fibrillar-like formation was finally examined by a fluorescence analysis following the increase in fluorescence intensity of Thioflavin T (ThT), see Fig. 1d. BSA showed a rapid fibril formation when subjected to high temperatures. After 30 min, the normalised value of fluorescence intensity showed a 3-fold increase, reaching a 4-fold increase after 3 h, until it reached a plateau after about 5 h. These analyses align very well with the results obtained by STEM correlating the increase of protein clusters with an enhancement of ThT fluorescence intensity.

All results from standard analyses consistently affirm the formation and growth of BSA aggregates in the solution. Consequently, Ω was acquired on this set of samples. To ensure the reliability of our findings, each sample solution was prepared in triplicate, and the standard deviation was calculated. The results are presented in the graph in Fig. 1e, showing that spectral intensity increases with the duration of aggregation, distinguishing the spectral curve for each solution. Notably, this increase is more prominent for the shorter wavelengths. Considering that DLS measurements indicate the size of BSA aggregates in the solution is much smaller than the wavelength of the incident light and that the curves in Fig. 1e exhibit λ^{-4} dependence, the origin of Ω wavelength dependence was attributed to the Rayleigh scattering on the aggregate particles. Further, the Rayleigh scattering of a single particle was analytically expressed. For additional details, refer to section Materials and Methods. The change of scatter numbers was estimated from geometry modelling aggregates as spheres and considering that the size of aggregates increases while the mass concentration remains constant. Utilising the DLS radius of the scattering particle before aggregation (4.43 nm) and combining the Rayleigh scattering of a

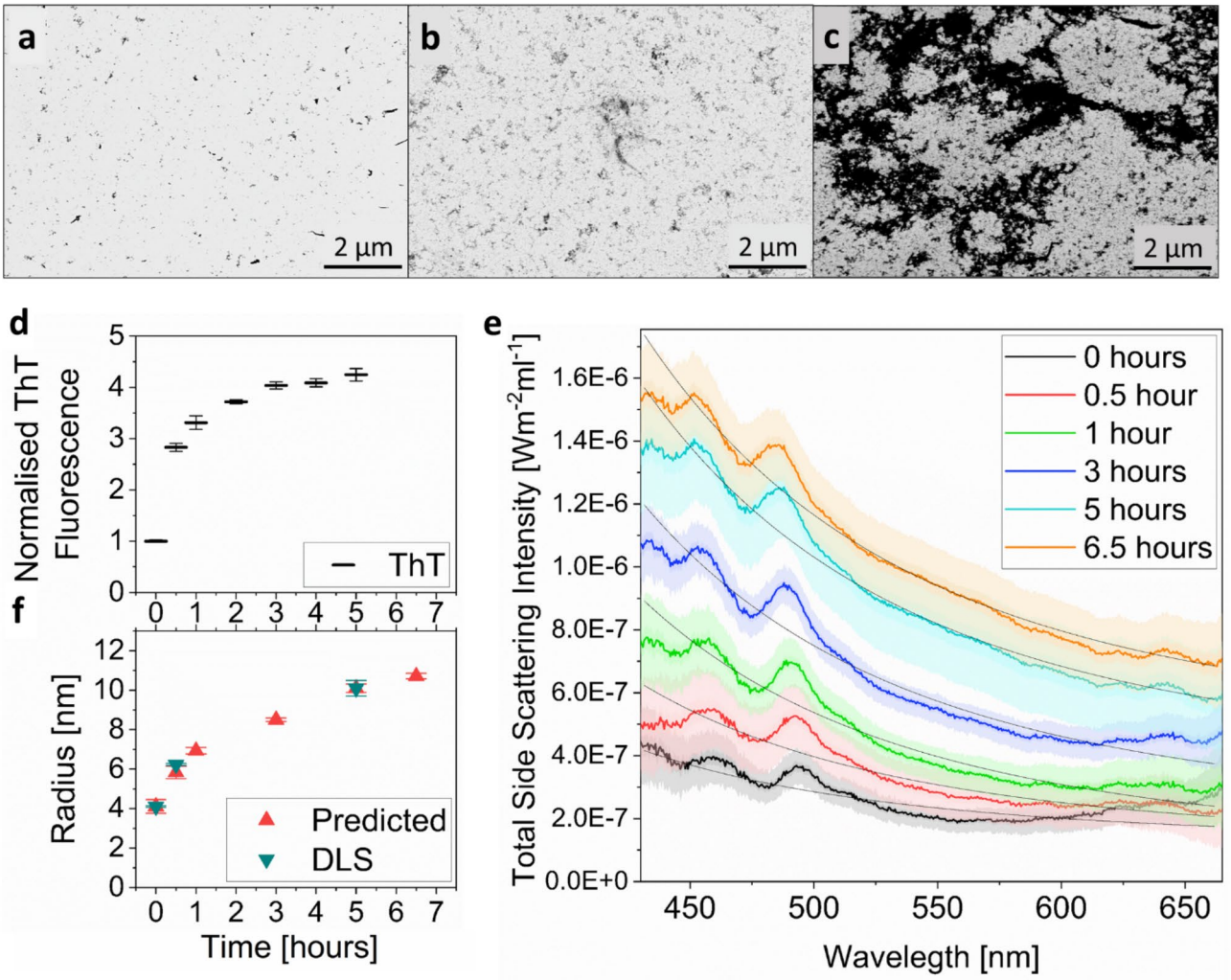

Fig. 1. Side Scattering Spectrum of BSA aggregates and complementary methods measurements. (**a–c**) BSA aggregations at different stages of fibrillation visualised by STEM after (**a**) 0, (**b**) 0.5 and (**c**) 5 h. (**d**) ThT fluorescence fibrillation analysis. (**e**) The total side scattering power Ω, lighter coloured areas represent standard error, and the black curves represent fit $y \sim \lambda^{-4}$. (**f**) Radius from DLS measurements and its estimation form Total Side Scattering Power.

single aggregate with the estimation of the change in their number, we were able to predict the radius of the aggregates from the scattering curves, as shown in Fig. 1f (Materials and Methods Eq. 11 and supplementary Table S1). The predicted sizes align well with two other DLS measurements and are fully consistent with trends observed in fluorescence experiments. This study demonstrates that the described method enables monitoring of the aggregation process, and the wavelength dependence of Ω contains information about the size and number of scattering particles, thus offering a means for size estimation.

Monitoring of Tau protein fibrillation

After analysing BSA aggregates and data interpretation, the customised side-scattering spectroscope was utilised to characterise and monitor Tau protein fibrillation and observe its Ω wavelength dependence that is expected to be expressed in the reflectance spectrum of AD human retina. As a representation of the fibrillation process occurring in AD, the microtubule-binding region of Tau protein, referred to as K18, was chosen. In vivo, in pathological conditions, the K18 region of Tau is subjected to an aberrant phosphorylation that leads to a conformational change. Tau forms oligomers, which subsequently assemble into neurofibrillary tangles and accumulate in the brain, leading to AD[36–42]. In vitro, to analyse the fibrillation mechanism and replicate the fibril structure, K18 protein is exposed to aggregation agents and polyanionic molecules that induce oligomerisation. The most used is heparin, a negatively charged sulphated glycosaminoglycan[43,44]. However, the use of heparin as a cofactor of Tau fibrillation may raise questions about its relevance to disease pathology and potential clinical implications due to its interaction with a wide range of proteins, which could lead to nonspecific effects[45,46]. Therefore, new aggregating agents have been analysed, and polyphosphates (polyP) gained great importance in the production and analysis of Tau fibrils. In fact, in vivo, polyP seems to be involved in the formation of Tau aggregates and in the development and progression of AD. In vitro, the exposure of K18 to polyP produces mature fibrils that lack the flaws of heparin-induced fibrils and show cytotoxicity and neurodegeneration in cells[47–49].

Sets of solutions with the same concentration of Tau protein were prepared to contain various stages of fibrillation by varying the incubation time starting from $t = 0$ in the total absence of inducer to 35 days of fibrillation upon incubation with a 4-fold excess of inducer. The first set of solutions was prepared for each fibrillation time in three replicas for scattering measurement, and the other two sets were prepared and used for ThT fluorescence, DLS, and STEM analysis. At first, the solutions were measured by the spectroscope, Ω was acquired for each fibrillation stage in three replicas. The average value of each curve and its standard error is printed in Fig. 2a. Similar to BSA, the Ω increases with the time of fibrillation more significantly at shorter wavelengths, although the shape of Ω curve varies from BSA. The solutions were analysed using standard methods to assign this wavelength dependence to the properties of the fibrils. The dimensions with the progress of aggregation were successfully determined by DLS analysis; in particular, the measured radius was (i) (140 ± 2) nm before fibrillation and (ii) (1800 ± 200) nm at 7 days of fibrillation. For the longer time after fibrillation (35 days), a significant intensity autocorrelation curve cannot be obtained due to sedimentation (Fig. 2c, blue curve). This is also evidenced by the low counts signal that significantly increases as the sample is shaken on and rapidly decreases again after a few seconds. For these proteins, DLS analysis also indicates that the samples are already polydisperse before fibrillation, with the polydispersity further increasing after 7 days. Similarly, fluorescence analysis of K18 using ThT was successful in monitoring the early stage of fibrillation. Indeed, following the typical initial lag phase necessary for nuclei formation[50,51], polyP expedites the fibril elongation. This acceleration is evident from the relative fluorescence of the samples, which exhibited a 4-fold increase compared to the non-fibrillated control after 4 days of exposure at 37 °C (Fig. 2b). After 7 days, an 8-fold increment of ThT relative fluorescence (Fig. 2b). However, after 1 month of fibrillation, the relative fluorescence showed no intensity increase when compared to the control (Fig. 2b). As evidenced by the DLS results and STEM images (Fig. 2f), it is probably due to the larger cluster density, which causes heavy precipitation and hampers measurements in the solution. STEM images confirmed the growth of Tau protein fibrils and reaching the size of a few micrometres. After 7 days, elongated mature fibrils that form complex tangles of ~1 µm were present (Fig. 2d, e). These results are in good agreement with DLS. Finally, after 30 days, these tangles combined into bigger amorphous aggregates, reaching dimensions higher than 5 µm (Fig. 2f).

DLS and STEM reported that the size of Tau protein fibrils is two orders of magnitude larger than BSA aggregates, demonstrating the capability of the newly developed side-scattering spectroscope to measure and correlate the scattering of particles from few nanometres to micrometre scale. The measured protein aggregates, simulating the Tau protein in AD-affected retinas, exhibit non-spherical shapes and significant size polydispersity in the solution, with sizes comparable to the wavelength of incident light. The higher complexity of the system influences the experimental data in Fig. 2a, as the scattering curve is a sum of complex scattering phenomena happening at various sizes and shapes of protein aggregates. Under these conditions, the Rayleigh scattering equation, applicable to nearly monodisperse nanometre-sized BSA aggregates, does not provide an accurate description of the observed scattering. Consequently, while the increase of intensity at shorter wavelengths is preserved, the Ω curves lack a distinguishable λ^{-4} dependence. The slope of scattering curves grows with fibrillation time, demonstrating that not only Ω increases but also the wavelength dependence is more prominent with growing fibril size. These results show that, although the trend of increased scattering at shorter wavelengths is more pronounced for smaller, nanosized particles like BSA (dependence), it also holds for larger, microsized particles contributing to the total scattering. This scattering behaviour is consistent with the phenomenon observed in the reflected spectrum of AD patients' retinas, encouraging the use of HSI imaging even for advanced stages of AD, as it can be expected that the micrometer-sized fibrils contribute to the spectral signature in the retina-reflected spectrum.

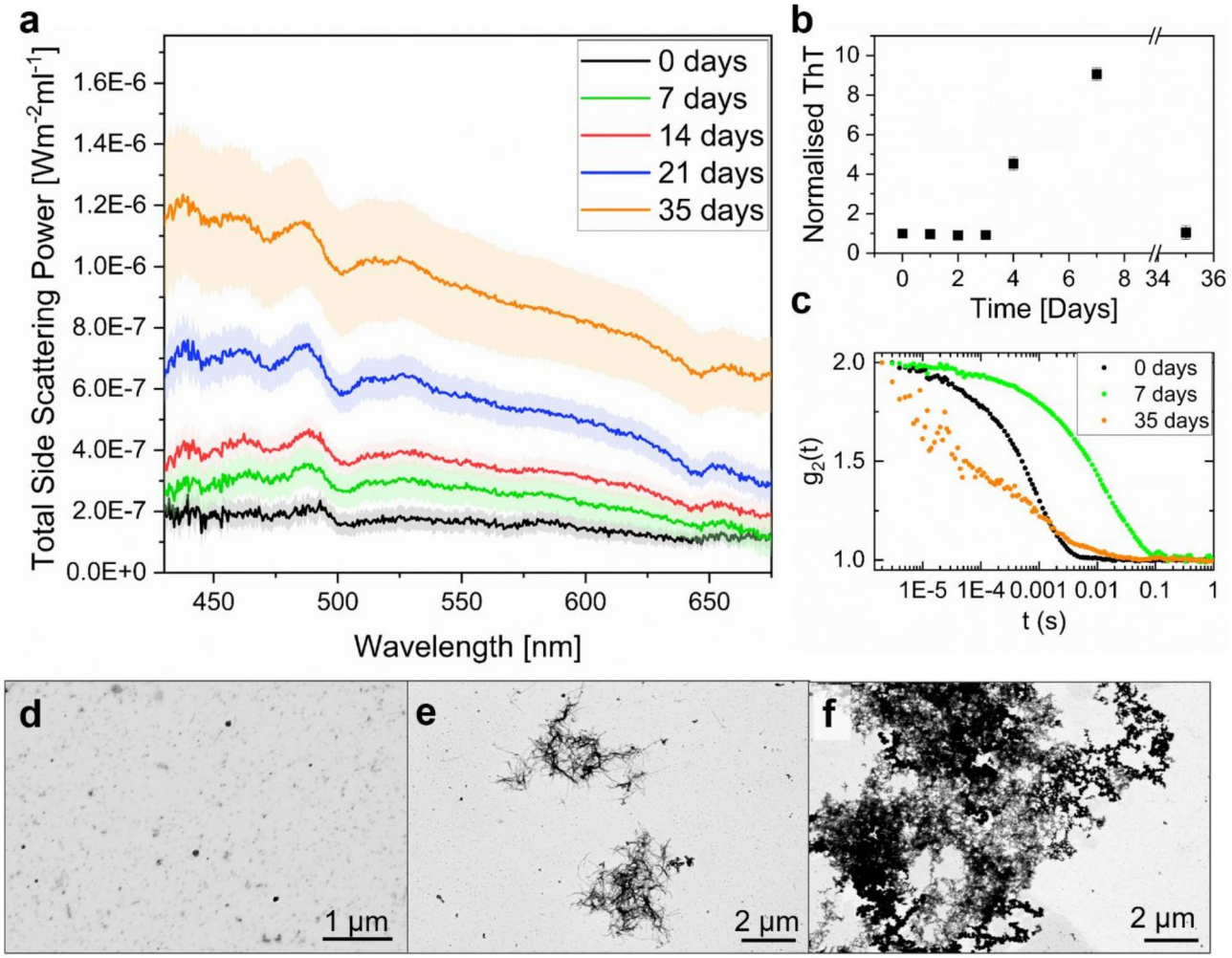

Fig. 2. Side scattering spectrum of tau protein fibrillation and fibrils STEM images. (**a**) Total side scattering power Ω measured for the solution containing Tau protein at various stages of fibrillation. The black line represents the linear fit of the scattering curve. (**b**) ThT fluorescence fibrillation analysis **c**DLS measurements. (**d–f**) Tau protein fibrils at different stages of fibrillation visualised by STEM after (**d**) 0, (**e**) 7 and (**f**) 35 days of fibrillation.

Discussion

Within this study, we have successfully developed and implemented a customised method tailored for monitoring the side-scattering of protein fibrils. The measured intensity was assigned to the physical properties of the scattering particles. This method was validated through the analysis of BSA aggregates, a well-characterised biological system known to undergo secondary structure changes, resulting in the formation of fibril-like aggregates. This was observed through standard measurement methods, such as DLS, STEM, and fluorescence intensity, which support both BSA structural insights and a clear correlation between alterations in protein structure and the binding of ThT[52]. Measured total side-scattering intensity grows with the aggregation time, demonstrating the suitability of the proposed technique for aggregation growth monitoring. Moreover, the measurement revealed that the spectral dependence of side-scattering power can be assigned to the scattering particle size.

As a main result, the scattering spectrum signature of Tau protein fibrils was measured at various fibrillation stages. The effect of Tau protein is less explored in HSI of AD retina than Aβ, while recent studies suggested that levels of phosphorylated Tau protein are more consistent with disease symptomatology than cerebral Aβ accumulation[27,53]. Our findings reveal that the measured total side-scattering spectra of Tau fibrils show a strict correlation with the formation of fibrillar structures, revealing alterations in the structure at an early stage, i.e. when aggregates in the nanoscale range are present, as supported by DLS and STEM analysis. Our results provide an excellent tool for identifying the scattering spectrum signatures observed in the brain and retina of AD patients. Moreover, the comparison of scattering measurements for Tau and BSA fibrillation demonstrates that the presented method can effectively monitor the fibrillation process of protein fibrils/aggregates with sizes of a few nanometres up to the micrometres, a range where other methods encounter difficulties.

The presented results connect the scattering properties of protein fibrils and the specific spectral signatures observed in retinal hyperspectral images of Alzheimer's patients. The increased side scattering we document leads to a decrease in backscattering, which is fully consistent with the observed increase in optical density in the blue spectrum for Alzheimer's patients[24]. Thus, our observed data demonstrate that the scattering of Tau protein fibrils mirrors the spectral signatures observed in the retinas of AD patients. These findings are crucial for advancing our understanding and refining hyperspectral imaging technology, bringing it a step closer to the development of a tool for screening Alzheimer's Disease in its preclinical stage. The detection of increasing protein fibril accumulation in the retina combined with other methods, such as classification of various retinal features influenced by AD or protein staining with specific florescent dye, etc., can increase the sensitivity and specificity of rapid, non-invasive AD diagnosis. This multimodal approach can then be used before symptoms of AD are detected by existing methods (e.g., dementia assessment tests) to select a cohort with a higher probability of AD development, facilitating the testing of newly developed drugs aiming to stop AD progression before irreversible neurodegenerative changes occur, inducing cognitive decline of the subject.

Materials and methods

Light side scattering spectroscopy

Experimental setup design

The custom bench optical setup was designed to acquire the scattering spectrum of protein aggregates, utilising a minimal sample solution volume, typically within the range of a few hundred microliters. The sketch of the experimental setup is visualised in Fig. 3. The subtraction of the reflection of the source light from optical components is a critical procedure to achieve an unbiased measurement of the side scattering spectrum, especially as the scattered light intensity is much lower than the source. Thus, our experiment has been designed to incorporate a series of advantageous features, such as the minimisation of the required liquid volume and reduced effects from cell reflections.

Optical path for light source The light source, an OSL2 Fiber Illuminator (Thorlabs, Inc.), passes through an optical path that includes a field lens (L1) and lens a preliminary collimating lens (L2). Then, the light is focused (with L3) onto a pinhole, where the light outside of the focal point is truncated for further collimation thanks to objective (obj1). The collimated beam is polarised and ultimately focused into the capillary containing the sample. This system ensures a homogeneous light spot in the sample solution with a diameter of 0.6 mm and irradiance of 3 W/m^2, allowing it to enter the capillary without interacting with its sidewalls. Here, the incident light interacts with the particles in the solution.

Disposable capillaries and customised holder A customised holder for capillaries was designed and 3D printed, enabling microliter volume analysis. Moreover, the holder geometry ensures capillary self-alignment. The used Hollow Square Borosilicate Glass Capillaries ID 0.80 × 0.80 mm (CM Scientific Ryefield (EU) Ltd.) were disposed of after each experiment to prevent contamination and thus maintain measurement reproducibility and accuracy.

Spectra acquisition and focus monitoring After the interaction of light with the sample solution, the light passes through two separated optical paths, which are selected through a removable mirror (M4): (i) back-reflected light and (ii) side-scattered light collected by objective (Obj2) perpendicular to the incoming light. At both paths, the light passes through a polariser (analyser) to further eliminate the residual specular reflected light. Back-reflected light enables monitoring of the light spot position in the capillary on camera (C1) before and during the experiment while obtaining the spectral image at the second camera (C2). The spectral image is created in the spectrometer part of the setup composed of slit (100 μm), reflective grating (Thorlabs, Inc.) and then the second camera, where is acquired the spectral image (x vertical location, y spectrum). Spectrum wavelength was calibrated with spectral measurement, where broad wavelength light source was filtered with multiple bandpass filters, enabling the mapping of C2 camera pixels with selected wavelength lines. Before the start of each measurement, a dark and white spectrum is used to normalise spectra (Eq. 1). As a white sample, a spectrum of 20 mg/ml of ZnO in a water solution was acquired. The background signal, acquired by analysing PBS (Phosphate Buffered Saline) solution, is subtracted from the sample spectra:

$$Sample\ Spectrum = \frac{\left(\frac{Sample}{exposure}\right)-\left(\frac{Dark}{exposure}\right)}{\left(\frac{White}{exposure}\right)-\left(\frac{Dark}{exposure}\right)} - \frac{\left(\frac{PBS}{exposure}\right)-\left(\frac{Dark}{exposure}\right)}{\left(\frac{White}{exposure}\right)-\left(\frac{Dark}{exposure}\right)}\# \quad (1)$$

Total side scattering power calculation

The system has been calibrated by measuring the side scattering intensity of solutions containing various concentrations of Polystyrene beads (PS beads). The PS beads have been chosen for our calibration as their scattering cross section can be calculated analytically as Mie scattering. Before the measurement of scattering, the calculations were conducted using MiePlot v4.6 computer program (Supplementary Fig. S2). Afterwards, the solutions of PS beads were analysed in the build side-scattering spectroscope, and the range of concentration where a single scattering occurs was determined (Supplementary Fig. S1), as in this range, a linear growth of intensity with PS beads concentration is observed. The scattering of a single bead was calculated and used as a normalisation constant in the following calculations, where the measured intensity was attributed to the physical properties of scattering particles in the solution. The measured intensity of PS beads in the solution can be expressed with the following equation:

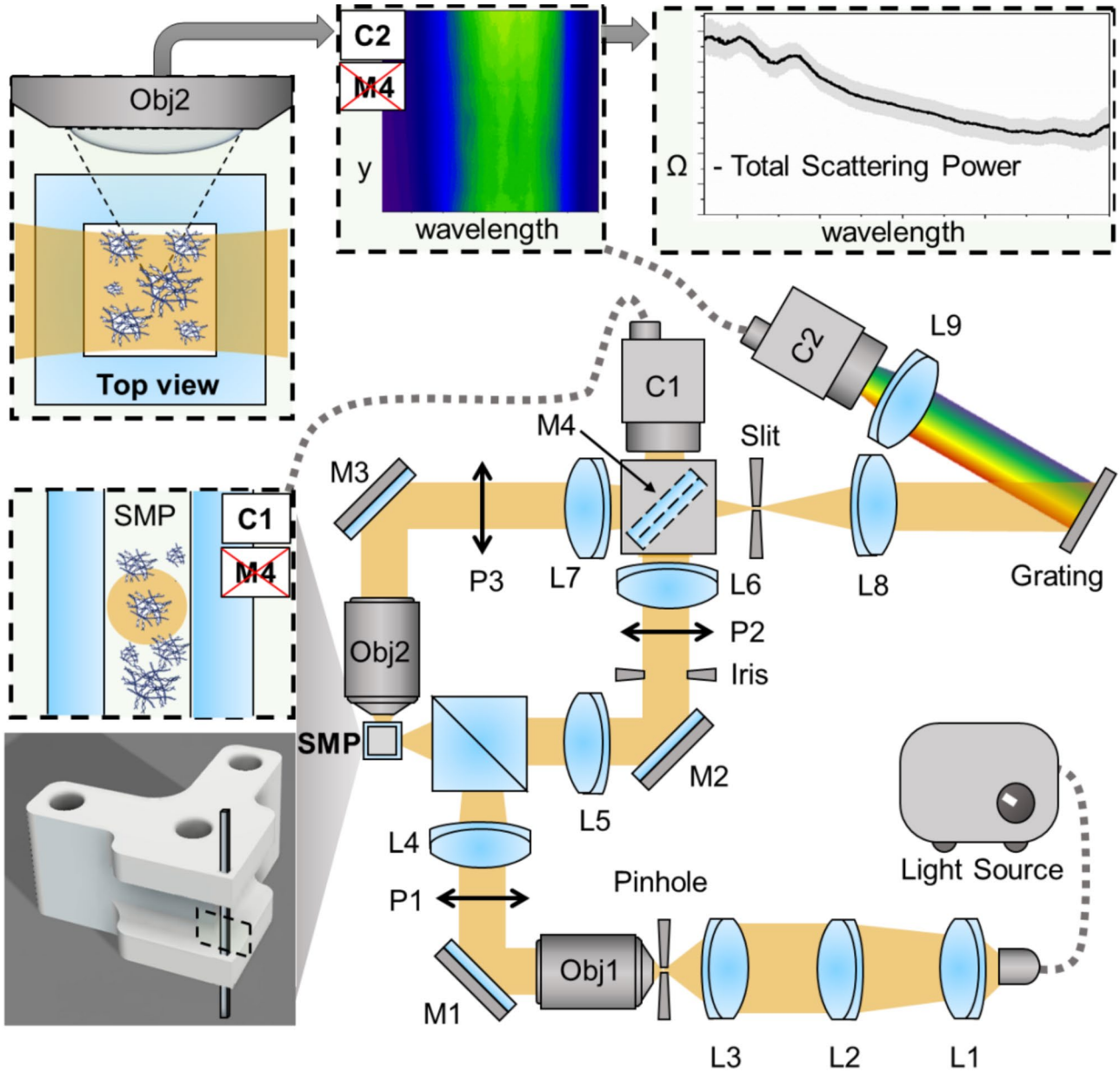

Fig. 3. Design of experimental setup. The presented setup is composed of the following components: Light Source; 9 achromatic lenses with focal lengths of 25 mm (L1, L3), 100 mm (L2), 50 mm (L4, L8, L9) and 75 mm (L5, L6, L7); 2 objectives (Obj1) and (Obj2); 4 mirrors M1, M2, M3 and removable mirror M4; 3 linear polariser filter P1, P2 and P3; customised 3D printed capillary holder; Pinhole; Iris; Slit; Grating and 2 cameras (C1 and C2). All the optical components are suitable for the 400–700 nm wavelength range.

$$I_{exp}^{PSbeads} = n_{PSbeads} V I_{\mathrm{S}}^{PSbeads} \tag{2}$$

where $\sigma_{90}^{PSbeads}$ is cross-section scattering at 90 degrees calculated by Mie theory (Supplementary fig. S2), n particle number concentration, V volume of solution participating in scattering, I_{exp} detected intensity.

A similar equation can be written for the measured intensity of any scattering particles in the solution:

$$I_{exp}^{Protein} = n_{Protein} V I_{\mathrm{S}}^{Protein} \tag{3}$$

where $I_{\mathrm{S}}^{Protein}$ is the unknown scattering intensity of measured particles and $n_{Protein}$is their concentration., By combining the Eqs. (2) and (3), we obtain the multiplication of $I_{\mathrm{S}}^{Protein}$ and $n_{Protein}$, which we call total side scattering power Ω and it is defined by the following equation:

$$\Omega = I_{\mathrm{S}}^{Protein} n_{Protein} = \frac{I_{exp}^{Protein} n_{PSbeads} I_{\mathrm{S}}^{PSbeads}}{I_{exp}^{PSbeads}} = I_{exp}^{Protein} k\# \tag{4}$$

where k is the constant assigning the measured intensity value physical interpretation—the Ω is expressed as a total side scattering intensity of the system, so how much is scattering at the given angle per liquid volume.

Aggregation size estimation with Rayleigh scattering

During the aggregation process, the mass concentration of aggregating molecules is constant, as also the aggregates' density; thus, its total molecules' volume V_0 at the initial aggregating stage is equal to the total volume in the following stage V_x:

$$V_0 = V_x \tag{5}$$

We approximate the shape of the aggregate as a sphere with an initial radius r_0, so the total volume is equal to the volume of a single sphere multiplied by their initial number N_0, and this is equal to the volume of an aggregating particle (a single particle is resulting from a set of aggregated molecules) at different aggregation times with radius r_x multiplied by their number N_x:

$$\tfrac{4}{3}\pi\, r_0^3 N_0 = \tfrac{4}{3}\pi\, r_x^3 N_x \tag{6}$$

Then, the change in particle number can be calculated by the following equation:

$$N_x = \left(\tfrac{r_0}{r_x}\right)^3 N_0 \tag{7}$$

The number of particles at the initial aggregation stage can also be expressed as the ratio between their measured total side scattering power Ω_0 and the calculated side-scattering of a single scattering particle at the initial stage I_{s_0}:

$$N_0 = \tfrac{\Omega_0 V}{I_{s_0}} = \frac{\Omega_0 V}{\int_{\phi_1}^{\phi_2} I_0 \frac{1+\cos^2\phi}{2R^2}\left(\frac{2\pi}{\lambda}\right)^4\left(\frac{n^2-1}{n^2+2}\right)^2 r_0{}^6 d\phi} \tag{8}$$

The general measured total side scattering power Ω can be expressed as the number of particle N_x multiplied by the side-scatteing of a single particle I_s:

$$\Omega = \tfrac{N_x I_s}{V} = \left(\tfrac{r_0}{r_x}\right)^3 \tfrac{N_0}{V} \int_{\phi_1}^{\phi_2} I_0 \tfrac{1+\cos^2\phi}{2R^2}\left(\tfrac{2\pi}{\lambda}\right)^4\left(\tfrac{n^2-1}{n^2+2}\right)^2 r_x{}^6 d\phi \tag{9}$$

where I_0 is the intensity of source light, λ is the wavelength of light, n is the refractive index of aggregates, R is the distance from the scattering particle and ϕ_1, and ϕ_2 are detection limit angles defined by the numerical aperture of the objective (Fig. 3—Obj2). By combining Eqs. (8) and (9), we obtain an expression for the estimation of scattering particle radius with the known initial radius r_0 :

$$r_x = r_0 \frac{\sqrt[3]{\Omega}}{\sqrt[3]{\Omega_0}} \tag{10}$$

Sample preparation

Model protein BSA fibrillation and analysis

A model protein was used as a control to validate the instrumental setup. Bovine serum albumin (BSA) is known to rapidly form aggregates when subjected to high temperatures[54]. Therefore, BSA 400 µM was kept at 63 °C for from 30 min up to 6 h. Before the analysis with the instrument, the fibrillation was confirmed using thioflavin T (ThT) fluorescence, dynamic light scattering (DLS), and scanning transmission electron microscopy (STEM).

Tau protein construct design and expression

This study used the K18 domain of Tau isoform 0N4R, which contains 4 microtubule-binding repeats (MTBR) extending from residues 244 to 372. The native cysteine 291 in Tau K18 was modified to alanine to prevent the formation of disulfide bonds and enhance the purification of the construct, given that many studies confirmed that the formation of intermolecular disulfide bridges is not required for dimerisation[55–57]. The genes coding for K18 were cloned into a pET30a vector. The plasmid was inserted in *Escherichia coli* cells, and recombinant protein expression was induced using isopropyl β-D-1-tiogalattopiranoside (IPTG). *E. coli* cultures containing the recombinant protein were purchased from Genscript Biotech Corporation®.

Recombinant K18 extraction

To extract the protein, 20 g of collected cells were resuspended in 100 mL of lysis buffer (20 mM MES, 1 mM EDTA, 0.2 mM $MgCl_2$, 300 mM NaCl, protease inhibitor, and DNAse, pH 6.4). Lysis was performed at 50% amplitude for 30 min, 3 s ON and 6 s OFF on ice. The lysate was centrifuged at 10,000 rpm for 30 min at 4 °C. The supernatant was separated from the cell debris and was then heated at 80 °C for 20 min to promote the precipitation of most of the undesired *E. coli* proteins. After this step, the sample was centrifuged again at 10,000 rpm for 30 min at 4 °C. The pellet containing the precipitated proteins was separated from the supernatant. Finally, dialysis was performed to exchange the buffer and prepare the sample for protein purification. The sample was inserted in a dialysis tubing cellulose membrane and left in 2 L of dialysis buffer (20 mM MES, 50 mM NaCl, 1 mM EDTA, 1 mM $MgCl_2$, pH 6.4) overnight at 4 °C. The next day, the sample was centrifuged at

10,000 rpm for 30 min at 4 °C for the last time. The supernatant was then collected and sterilised with a 0.22 µm syringe filter.

Recombinant K18 purification
The recombinant K18 was purified via two-step chromatography. The first step was a cation exchange chromatography, using a HiPrep™ SP HP 16/10 column (Cytiva) set on an ÄKTA® Pure (Cytiva) chromatograph. Buffer A was 20 mM MES, 1 mM EDTA, 1 mM MgCl2, 50 mM NaCl, while Buffer B was 20 mM MES, 1 mM EDTA, 1 mM $MgCl_2$, 1 M NaCl. The method was: 2 CV 15% Buffer B, 2 CV 30% Buffer B, 2 CV 40% Buffer B, 2 CV 45% Buffer B, 2 CV 50% Buffer B and 2 CV 100% Buffer B. The final chromatogram was examined, and the selected elution fractions were analysed by gel electrophoresis. The bands on the gel allowed for the selection of the fractions containing the protein of interest. Those fractions were selected and prepared for the second chromatographic step, size exclusion chromatography. The column used was a HiLoad™ 26/600 Superdex 75 (GE Healthcare). Buffer A was H_2O, Buffer B was PBS, and the method was: 2 CV 100% Buffer B. The final concentration of recombinant K18 was determined via UV-Vis spectrophotometry. The molar extinction coefficient ε for K18 at 270 nm is 1490 M^{-1} cm^{-1}. The final yield was 60 mg for 20 g of bacterial paste.

Recombinant K18 fibril preparation
Recombinant K18 400 µM in PBS was reduced using tris(2-carboxyethyl)phosphine (TCEP) 4 mM for 10 min at 55 °C. Subsequently, the aggregation agent sodium tripolyphosphate 1600 µM was added to initiate K18 protein aggregation in vitro. The samples were kept at 37 °C under rotation at 150 rpm. The protein was collected at multiple time points, 4 days, 1 week, 2 weeks, 3 weeks, and 5 weeks, and analysed via dynamic light scattering (DLS) and scanning transmission electron microscopy (STEM) to confirm the presence of fibrils.

Protein fibrillation analysis

Thioflavin T (ThT) fluorescence
To monitor the fibrillation kinetics of BSA and K18, a fluorescence analysis was performed. A widely used fluorophore, ThT, was selected. The fluorophore stock was prepared by resuspending 2 mg of powder in 1 mL of PBS, and the final concentration was calculated by UV-vis measurements using $\varepsilon_{420} = 31{,}600\ M^{-1}\ cm^{-1}$. For BSA, ThT 20 µM was added to 400 µL of BSA 400 µM kept at 63 °C. Multiple time points were analysed: 0.5, 1, 2, 3, 4, 5, 20, and 24 h. One sample was left at RT and used as a control. For K18, ThT 20 µM was added to 400 µL of K18 400 µM fibrillated, as shown above. Multiple time points were analysed: 1, 2, 3, 4, 7, and 30 days. One sample was left at RT and used as a control. Fluorescence was measured using excitation at 420 nm and emission at 485 nm. All the measurements were made by using the RF-6000 fluorimeter (Shimadzu RF-6000).

Dynamic light scattering (DLS)
DLS measurements were performed using a logarithmic correlator in combination with a homemade optical set-up[58]. The monochromatic and polarised beam of a He–Ne (λ = 632.8 nm) 10 mW laser is focused on the sample cuvette placed in a cylindrical glass cell filled with water for index matching and temperature control. The scattered light is focused in the core of a single-mode optical fibre that permits to obtain a very high coherence factor. The number of detected photons, measured from a Perkin Elmer photomultiplier used in single photon counting mode, is transferred to a computer through an input-output digital card from National Instruments®. The intensity autocorrelation functions is directly computed using a software correlator as $g_2(q, t) = \langle I(q, t) I(q, 0)\rangle / \langle I(q, 0)\rangle^2$, where q is the modulus of the scattering vector defined as $q = (4\pi n/\lambda)\sin(\theta/2)$ (where n is the refractive index of the solvent and θ is the scattering angle, θ = 90° in the present experiment). The raw measurements, as directly obtained, without any data corrections, are shown in Fig. 2c for K18 samples before fibrillation and at different times after fibrillation (coloured symbols as described in the legend). Quantitative analysis of the measurements was obtained through a fit of the data with a conventional Kohlrausch–Williams–Watts expression:

$$g_2(t) = 1 + be^{-\left(\frac{2t}{\tau}\right)^{\beta}}$$

where b is the coherence factor, τ is the relaxation time related to the motion of the particles and β the shape parameters connected to the sample polydispersity. In the case of dilute samples, as measured in the present manuscript, the radius of the particles can be calculated according to the Stokes–Einstein relation as $R = K_BT/6\pi\eta D$, where D is the translational diffusion coefficient calculated from τ through the relation $\tau = 1/q^2D$. Measurements have been performed at T = 20 °C K for BSA and T = 25 °C K for K18 samples while sample viscosity η has been approximated with the solvent one[59].

Scanning transmission electron microscopy (STEM)
To characterise the fibrils, STEM images of BSA and K18 were produced and analysed. BSA 100 µM was prepared as shown above. Time points 0.5 and 5 h were selected, plus the control was not subjected to high temperature. K18 100 µM was also prepared as described previously. The selected time points were 1 week and 4 weeks, plus a control not put at 37 °C. The samples were prepared for STEM imaging. The samples were diluted with H_2O from 100 to 50 µM. One drop of sample was loaded onto a carbon-coated 3 mm copper grid. The sample was left to adsorb for 3 min. The grid was washed with one drop of water for 3 min. Then, one drop of the staining solution uranyl acetate 3% was added and left for 3 min. The grid was washed twice with H_2O for 3 min. All samples were visualised using a Zeiss Auriga microscope used in STEM mode.

Data availability

Sequence data that support the findings of this study have been deposited in the https://github.com/SalajkovaZita/DataFile.gitrepository.

Received: 9 July 2024; Accepted: 28 February 2025
Published online: 06 March 2025

References

1. Sweeney, P. et al. Protein misfolding in neurodegenerative diseases: implications and strategies. *Transl. Neurodegener.* **6**, 1–13. https://doi.org/10.1186/s40035-017-0077-5 (2017).
2. Brier, M. R. et al. Tau and Ab imaging, CSF measures, and cognition in Alzheimer's disease. *Sci. Transl. Med.* **8**, 1–10. https://doi.org/10.1126/scitranslmed.aaf2362 (2016).
3. Bateman, R. J. et al. Clinical and biomarker changes in dominantly inherited Alzheimer's disease. *N. Engl. J. Med.* **367**, 795–804. https://doi.org/10.1056/nejmoa1202753 (2012).
4. Jack, C. R. et al. Hypothetical model of dynamic biomarkers of the Alzheimer's pathological cascade. *Lancet Neurol.* **9**, 119–128. https://doi.org/10.1016/S1474-4422(09)70299-6 (2010).
5. Sperling, R. A. et al. Toward defining the preclinical stages of Alzheimer's disease: recommendations from the National Institute on aging-Alzheimer's association workgroups on diagnostic guidelines for Alzheimer's disease. *Alzheimer's Dement.* **7**, 280–292. https://doi.org/10.1016/J.JALZ.2011.03.003 (2011).
6. Marcus, C., Mena, E. & Subramaniam, R. M. Brain PET in the diagnosis of Alzheimer's disease. *Clin. Nucl. Med.* **39**, e413. https://doi.org/10.1097/RLU.0000000000000547 (2014).
7. Hampel, H. et al. State-of-the-art of lumbar puncture and its place in the journey of patients with Alzheimer's disease. *Alzheimer's Dement.* **18**, 159–177 (2022).
8. Thientunyakit, T. et al. Relationships between amyloid levels, glucose metabolism, morphologic changes in the brain and clinical status of patients with Alzheimer's disease. *Ann. Nucl. Med.* **34**, 337–348. https://doi.org/10.1007/s12149-020-01453-y (2020).
9. Weller, J. & Budson, A. Current Understanding of Alzheimer's disease diagnosis and treatment. *F1000Research* **7**, 1. https://doi.org/10.12688/F1000RESEARCH.14506.1 (2018).
10. Mossello, E. & Ballini, E. Management of patients with Alzheimer's disease: Pharmacological treatment and quality of life. *Ther. Adv. Chronic Dis.* **3**, 183–193. https://doi.org/10.1177/2040622312452387 (2012).
11. Mirzaei, N. et al. Alzheimer's retinopathy: seeing disease in the eyes. *Front. Neurosci.* **14**, 921. https://doi.org/10.3389/FNINS.2020.00921 (2020).
12. Grimaldi, A. et al. Neuroinflammatory processes, A1 astrocyte activation and protein aggregation in the retina of Alzheimer's disease patients, possible biomarkers for early diagnosis. *Front. Neurosci.* **13**, 925. https://doi.org/10.3389/fnins.2019.00925 (2019).
13. Hart de Ruyter, F. J. et al. Phosphorylated Tau in the retina correlates with Tau pathology in the brain in Alzheimer's disease and primary tauopathies. *Acta Neuropathol.* **145**, 197–218. https://doi.org/10.1007/s00401-022-02525-1 (2023).
14. Grimaldi, A. et al. Inflammation, neurodegeneration and protein aggregation in the retina as ocular biomarkers for Alzheimer's disease in the 3xTg-AD mouse model. *Cell. Death Dis.* **9**, 5. https://doi.org/10.1038/s41419-018-0740-5 (2018).
15. More, S. S., Beach, J. M. & Vince, R. Early detection of amyloidopathy in Alzheimer's mice by hyperspectral endoscopy. *Investig. Ophthalmol. Vis. Sci.* **57**, 3231–3238. https://doi.org/10.1167/IOVS.15-17406 (2016).
16. Selkoe, D. J. & Hardy, J. The amyloid hypothesis of Alzheimer's disease at 25 years. *EMBO Mol. Med.* **8**, 595–608. https://doi.org/10.15252/emmm.201606210 (2016).
17. Guo, L. Alzheimer's disease and retinal neurodegeneration. *Curr. Alzheimer Res.* **999**, 1–6. https://doi.org/10.2174/1567209197155452050 (2009).
18. Gupta, V. B. et al. Retinal changes in Alzheimer's disease—integrated prospects of imaging, functional and molecular advances. *Prog. Retin. Eye Res.* **82**, 100899 (2021).
19. Hadoux, X. et al. Non-invasive in vivo hyperspectral imaging of the retina for potential biomarker use in Alzheimer's disease. *Nat. Commun.* **10**, 1. https://doi.org/10.1038/S41467-019-12242-1 (2019).
20. Koronyo, Y. et al. Retinal amyloid pathology and proof-of-concept imaging trial in Alzheimer's disease. *JCI Insight* **2**, 21. https://doi.org/10.1172/JCI.INSIGHT.93621 (2017).
21. Koronyo-Hamaoui, M. et al. Identification of amyloid plaques in retinas from Alzheimer's patients and noninvasive in vivo optical imaging of retinal plaques in a mouse model. *Neuroimage* **54**, 20. https://doi.org/10.1016/j.neuroimage.2010.06.020 (2011).
22. Koronyo, Y., Salumbides, B. C., Black, K. L. & Koronyo-Hamaoui, M. Alzheimer's disease in the retina: imaging retinal Aβ plaques for early diagnosis and therapy assessment. *Neurodegener. Dis.* **10**, 285–293. https://doi.org/10.1159/000335154 (2012).
23. Garcia-Alloza, M. et al. Curcumin labels amyloid pathology in vivo, disrupts existing plaques, and partially restores distorted neurites in an alzheimer mouse model. *J. Neurochem.* **102**, 1095–1104. https://doi.org/10.1111/j.1471-4159.2007.04613.x (2007).
24. More, S. S. et al. In vivo assessment of retinal biomarkers by hyperspectral imaging: early detection of Alzheimer's disease. https://doi.org/10.1021/acschemneuro.9b00331 (2019).
25. More, S. S. & Vince, R. Hyperspectral imaging signatures detect amyloidopathy in alzheimers mouse retina well before onset of cognitive decline. *ACS Chem. Neurosci.* **6**, 306–315. https://doi.org/10.1021/CN500242Z/SUPPL_FILE/CN500242Z_SI_001.PDF (2015).
26. Chiquita, S. et al. The retina as a window or mirror of the brain changes detected in Alzheimer's disease: critical aspects to unravel. *Mol. Neurobiol.* **56**, 5416–5435. https://doi.org/10.1007/s12035-018-1461-6 (2019).
27. Alber, J. et al. Developing retinal biomarkers for the earliest stages of Alzheimer's disease: what we know, what we don't, and how to move forward. *Alzheimer's Dement.* **16**, 229–243. https://doi.org/10.1002/alz.12006 (2020).
28. Chang, S., Krzyzanowska, H. & Bowden, A. K. Label-free optical technologies to enhance noninvasive endoscopic imaging of early-stage cancers. *Annu. Rev. Anal. Chem.* **17**, 289–311. https://doi.org/10.1146/annurev-anchem-061622-014208 (2024).
29. Pleskow, D. K. et al. In vivo detection of bile duct pre-cancer with endoscopic light scattering spectroscopy. *Nat. Commun.* **14**, 7. https://doi.org/10.1038/s41467-022-35780-7 (2023).
30. Bassler, M. C. et al. Comparison of whiskbroom and pushbroom darkfield elastic light scattering spectroscopic imaging for head and neck cancer identification in a mouse model. *Anal. Bioanal. Chem.* **413**, 7363–7383. https://doi.org/10.1007/s00216-021-03726-5 (2021).
31. Zhang, L. et al. Light scattering spectroscopy identifies the malignant potential of pancreatic cysts during endoscopy. *Nat. Biomed. Eng.* **1**, 40. https://doi.org/10.1038/s41551-017-0040 (2017).
32. Vetri, V. et al. Bovine serum albumin protofibril-like aggregates formation: solo but not simple mechanism. *Arch. Biochem. Biophys.* **508**, 13–24. https://doi.org/10.1016/j.abb.2011.01.024 (2011).
33. Biancalana, M. & Koide, S. Molecular mechanism of Thioflavin-T binding to amyloid fibrils. *Biochim. Biophys. Acta Proteins Proteom.* **1804**, 1405–1412. https://doi.org/10.1016/j.bbapap.2010.04.001 (2010).
34. Adel, A., Nadia, M., Mohamed, O. & Abdelhafidh, G. Study of thermally and chemically unfolded conformations of bovine serum albumin by means of dynamic light scattering. *Mater. Sci. Eng. C* **28**, 594–600. https://doi.org/10.1016/j.msec.2007.10.004 (2008).

35. Dasgupta, M. & Kishore, N. Selective inhibition of aggregation/fibrillation of bovine serum albumin by osmolytes: mechanistic and energetics insights. *PLoS ONE* **12**, 1–26. https://doi.org/10.1371/journal.pone.0172208 (2017).
36. Gustke, N. et al. Domains of T protein and interactions with microtubules. *Biochemistry* **33**, 9511–9522. https://doi.org/10.1021/bi00198a017 (1994).
37. Mukrasch, M. D. et al. Sites of Tau important for aggregation populate β-structure and bind to microtubules and polyanions. *J. Biol. Chem.* **280**, 24978–24986. https://doi.org/10.1074/jbc.M501565200 (2005).
38. Li, W. et al. Inhibition of Tau fibrillization by oleocanthal via reaction with the amino groups of Tau. *J. Neurochem.* **110**, 1339–1351. https://doi.org/10.1111/j.1471-4159.2009.06224.x (2009).
39. Yu, W. et al. A critical role for the PAR-1/MARK-tau axis in mediating the toxic effects of Aβ on synapses and dendritic spines. *Hum. Mol. Genet.* **21**, 1384–1390. https://doi.org/10.1093/hmg/ddr576 (2012).
40. Von Bergen, M. et al. The core of tau-paired helical filaments studied by scanning transmission electron microscopy and limited proteolysis. *Biochemistry* **45**, 6446–6457. https://doi.org/10.1021/bi052530j (2006).
41. Shammas, S. L. et al. A mechanistic model of Tau amyloid aggregation based on direct observation of oligomers. *Nat. Commun.* **6**, 8025. https://doi.org/10.1038/ncomms8025 (2015).
42. Chiti, F. & Dobson, C. M. Protein misfolding, amyloid formation, and human disease: A summary of progress over the last decade. *Annu. Rev. Biochem.* **86**, 27–68. https://doi.org/10.1146/annurev-biochem-061516-045115 (2017).
43. Fichou, Y. et al. Tau-cofactor complexes as Building blocks of Tau fibrils. *Front. Neurosci.* **13**, 1–15. https://doi.org/10.3389/fnins.2019.01339 (2019).
44. Lo, C. H. Heterogeneous Tau oligomers as molecular targets for Alzheimer's disease and related Tauopathies. *Biophysica* **2**, 440–451. https://doi.org/10.3390/biophysica2040039 (2022).
45. Zhang, W. et al. Heparin-induced Tau filaments are polymorphic and differ from those in Alzheimer's and Pick's diseases. *Elife* **8**, 584. https://doi.org/10.7554/ELIFE.43584 (2019).
46. Fichou, Y. et al. Heparin-induced Tau filaments are structurally heterogeneous and differ from Alzheimer's disease filaments. *Chem. Commun.* **54**, 4573–4576. https://doi.org/10.1039/C8CC01355A (2018).
47. Lempart, J. & Jakob, U. Role of polyphosphate in amyloidogenic processes. *Cold Spring Harb. Perspect. Biol.* **11**, 41. https://doi.org/10.1101/cshperspect.a034041 (2019).
48. Lempart, J. et al. Mechanistic insights into the protective roles of polyphosphate against amyloid cytotoxicity. *Life Sci. Alliance* **2**, 1–13. https://doi.org/10.26508/lsa.201900486 (2019).
49. Jucker, M. & Walker, L. C. Self-propagation of pathogenic protein aggregates in neurodegenerative diseases. *Nature* **501**, 45–51. https://doi.org/10.1038/nature12481 (2013).
50. Marek, P., Mukherjee, S., Zanni, M. T. & Raleigh, D. P. Residue-specific, real-time characterization of lag-phase species and fibril growth during amyloid formation: A combined fluorescence and IR study of p-cyanophenylalanine analogs of islet amyloid polypeptide. *J. Mol. Biol.* **400**, 878–888. https://doi.org/10.1016/j.jmb.2010.05.041 (2010).
51. Arosio, P., Knowles, T. P. J. & Linse, S. On the lag phase in amyloid fibril formation. *Phys. Chem. Chem. Phys.* **17**, 7606–7618. https://doi.org/10.1039/c4cp05563b (2015).
52. Sulatskaya, A. I., Kuznetsova, I. M. & Turoverov, K. K. Interaction of thioflavin T with amyloid fibrils: fluorescence quantum yield of bound dye. *J. Phys. Chem. B* **116**, 2538–2544. https://doi.org/10.1021/jp2083055 (2012).
53. Hanseeuw, B. J. et al. Association of amyloid and Tau with cognition in preclinical alzheimer disease: A longitudinal study. *JAMA Neurol.* **76**, 915–924. https://doi.org/10.1001/jamaneurol.2019.1424 (2019).
54. Soloperto, A. et al. Rational design and synthesis of a novel BODIPY-based probe for selective imaging of Tau tangles in human iPSC-derived cortical neurons. *Sci. Rep.* **12**, 1–15. https://doi.org/10.1038/s41598-022-09016-z (2022).
55. Karikari, T. K. et al. Preparation of stable Tau oligomers for cellular and biochemical studies. *Anal. Biochem.* **566**, 67–74. https://doi.org/10.1016/j.ab.2018.10.013 (2019).
56. Okuyama, K. et al. Linkage-dependent contribution of repeat peptides to self-aggregation of three- or four-repeat microtubule-binding domains in Tau protein. *FEBS J.* **275**, 1529–1539. https://doi.org/10.1111/j.1742-4658.2008.06312.x (2008).
57. Huvent, I. et al. A functional fragment of Tau forms fibers without the need for an intermolecular cysteine Bridge. *Biochem. Biophys. Res. Commun.* **445**, 299–303. https://doi.org/10.1016/j.bbrc.2014.01.161 (2014).
58. Ruzicka, B., Zulian, L. & Ruocco, G. Routes to gelation in a clay suspension. *Phys. Rev. Lett.* **93**, 1–4. https://doi.org/10.1103/PhysRevLett.93.258301 (2004).
59. Nigro, V. et al. Dynamical behavior of microgels of interpenetrated polymer networks. *Soft Matter* **13**, 5185–5193. https://doi.org/10.1039/c7sm00739f (2017).

Acknowledgements

This work was supported by MUR PRIN 2022 (CUP: 2022CFP7RF, to ML). This research was also funded by the D-Tails-IIT Joint Lab, the. GR iso supported by Project "National Center for Gene Therapy and Drugs based on RNA Technology" (CN00000041) financed by NextGenerationEU PNRR MUR—M4C2—Action 1.4-Call "Potenziamento strutture di ricerca e creazione di "campioni nazionali di R\&S (CUP J33C22001130001)". The research leading to these results was also supported by European Research Council through its Synergy grant program, project ASTRA (grant agreement No 855923), by European Innovation Council through its Pathfinder Open Programme, project ivBM-4PAP (grant agreement No 101098989) and by Regione LAZIO Lazio-Innova: POR FESR Lazio 2014–2020 (A0375-2020-36549, CUP: B85F20003340002 to ML and PB). The authors also acknowledge the resources and services provided by the Biobank of Santa Lucia Foundation, Rome.

Author contributions

Z.S. wrote the main manuscript text, conceived, performed and designed the experiments and analysed the data. L.B. wrote the part of the manuscript text and performed the experiments. P.B. designed the experiment and wrote part of the manuscript text. B.R. performed and designed the experiments and analysed the data. F.M. performed and designed the experiments and analysed the data. F.D.L. performed and designed the experiments and analysed the data. A.B. provided technical support and helped with data interpretation. V.R. provided technical support and helped with data interpretation. G.R. provided technical support and helped with data interpretation. M.L. designed the study, provided technical support, and helped with data interpretation.All authors reviewed the manuscript.The authors declare no competing interests.

Declarations

Competing interests
The authors declare no competing interests.

Additional information
Supplementary Information The online version contains supplementary material available at https://doi.org/10.1038/s41598-025-92565-w.

Correspondence and requests for materials should be addressed to Z.S. or L.B.

Reprints and permissions information is available at www.nature.com/reprints.

Publisher's note Springer Nature remains neutral with regard to jurisdictional claims in published maps and institutional affiliations.